

Sensitivity functions of transient electromagnetic methods

Niels B. Christensen¹

ABSTRACT

Any geophysical measurement is a filter through which the distribution of a certain physical parameter in the subsurface is seen, and the sensitivity function is a characteristic of the method that reveals the nature of this filter. Insight into the structural pattern of the sensitivity function pertaining to a certain transmitter-receiver configuration provides the geophysicist with an image that allows an immediate qualitative understanding of the characteristics of the method. The assets and shortcomings of different measuring configurations can be discussed and understood, and the sensitivity function permits qualified predictions about resolution characteristics of new configurations and measuring strategies. I evaluated a rapid and accurate method for calculating 3D sensitivity functions of a homogeneous half-space model for a wide variety of transient electromagnetic configurations using the central loop and an airborne offset loop configuration as examples. Computations of 3D sensitivity functions were performed as convolutions in the time domain between the electric fields from the transmitter and the receiver, had it been used as a transmitter. The 2D and 1D sensitivity functions are found through numerical integration of the 3D functions. Beside offering insight into the resolution capability of the measuring configuration, the sensitivity functions lend themselves to rapid calculations of approximate responses and derivatives in various modeling and inversion strategies.

INTRODUCTION

Electromagnetic (EM) methods, frequency and time domain, are used for a wide variety of purposes. Time-domain electromagnetic (TEM) methods — which are the subject of this paper — and in particular airborne systems, are increasingly used for mineral exploration (Paine, 2003; Macnae, 2007), all aspects of hydrogeophysical

mapping (Munday et al., 2004; Auken et al., 2006, 2009), saltwater intrusion (Fitterman and Deszcz-Pan, 1998; Jørgensen et al., 2012), bathymetry (Vrbancich and Fullagar, 2007), mapping of pollution (Hammack et al., 2002; Beamish and Mattson, 2003; Reid et al., 2012), geotechnical applications (Christensen and Reid, 2011), and a variety of other physical planning purposes (Thomsen et al., 2004). Over the past decades, in particular, helicopterborne TEM systems have been developed to provide early time measurements for improved near-surface resolution (Sørensen and Auken, 2004) and to increase the depth penetration (Nyboe et al., 2010; Nyboe and Sørensen, 2012).

Any geophysical measurement is a filter through which the distribution of a certain physical parameter in the subsurface is seen, and the sensitivity function is a characteristic of the method that reveals the nature of this filter; it could be described as the filter weights. Insight into the structural pattern of the sensitivity functions pertaining to a certain transmitter-receiver (Tx-Rx) configuration provides the geophysicist with an image that allows an immediate qualitative understanding of the characteristics of the method. It provides a set of concepts, in which assets and shortcomings of different measuring configurations can be discussed and understood from a perspective of a basic insight into the physics of diffusion of current into the ground. Knowledge of the sensitivity function also permits qualified predictions about new configurations and measuring strategies. A rapid and accurate method for calculating the sensitivity functions of a wide variety of configurations is, therefore, a very useful tool in the development of an understanding of the method and will be presented here.

A comprehensive study of the sensitivity functions of frequency-domain systems is given in Tølbøll and Christensen (2007). However, with a few exceptions (e.g., Hördt, 1998), less has been written about the sensitivity functions of transient electromagnetic systems, probably because it is numerically more challenging to calculate the sensitivity functions in the time domain than in the frequency domain. This paper will focus on the sensitivity functions of TEM systems.

From a historical perspective, approximations to sensitivity functions have been used to provide measures of the lateral and vertical

Manuscript received by the Editor 1 October 2013; revised manuscript received 25 January 2014; published online 18 July 2014.

¹University of Aarhus, Department of Earth Sciences, Aarhus, Denmark. E-mail: nbc@geo.au.dk.

© 2014 Society of Exploration Geophysicists. All rights reserved.

extent of the sensitivity, i.e., the footprint and depth of investigation of the method, respectively. Spies (1989) uses the vertical 1D sensitivity functions to estimate the depth of investigation of EM methods, and Liu and Becker (1990) and Reid and Vrbancich (2004) use an infinite-frequency approximation to estimate the lateral extent of the sensitivity function at the surface for a variety of frequency-domain configurations. Beamish (2003) formulates measures in the frequency domain that are an improvement over the infinite-conductivity estimates. These footprint measures rely on skin depth measures for vertical and horizontal magnetic dipole transmitters and the dependence on survey height, subsurface conductivity, and frequency is investigated.

A more comprehensive way of describing the general spatial resolution capabilities of EM systems than just considering integral measures like the footprint, is through the study of derivatives, or sensitivities (Chave, 1984; McGillivray and Oldenburg, 1990; Hördt, 1998). These sensitivities, which are basically the partial derivatives of EM data with respect to model parameters, describe how different parts of the earth contribute to the model response, and thus provide insight into the details of the spatial resolution capability and response characteristics of a given system, and their computation requires an accurate 3D sensitivity function to be available.

In least-squares inversion of EM data, the elements of the Jacobian are calculated as the integral of the sensitivity function over the model elements. Because of the challenges relating to computation time, often sensitivity functions of simpler models like a homogeneous half-space are used instead of the accurate sensitivity functions of the more complicated models used in the inversion. However, in several cases, such approximate derivatives will be quite sufficient to ensure convergence.

Boerner and Holladay (1990) derive an analytic expression for the 1D sensitivity function of a homogeneous half-space for frequency-domain methods for the tangential electric (TE) mode in which subsurface currents are parallel to the earth's surface. They show that the sensitivity function for a layered 1D model is well approximated by the half-space sensitivity function if the half-space conductivity is chosen equal to the apparent conductivity of the measurement. This is due to the fact that for the TE mode, the electric field is parallel to the layer boundaries of a 1D earth model and that the electric field, in contrast to the tangential magnetic (TM) mode, is only weakly model dependent. The TE and TM modes arise from a decomposition of the total EM field, e.g., through a formulation of Schelkunoff potentials (Ward and Hohmann, 1987). The scaling with the apparent conductivity makes the sensitivity adaptive in the sense that it reflects the skin depth of the actual measurement. These approximate sensitivities can be used for rapid computation of the elements of the Jacobian matrix of the inversion without degrading convergence performance.

Also in the case of TEM methods with Tx above ground, the electric field is parallel with the layer boundaries of a 1D earth and the sensitivity function is only weakly model dependent. The same adaptive modification can, therefore, be used in relation to TEM sensitivity functions for the homogeneous half-space.

Based on the observation that the sensitivity function can be regarded not only in a differential sense, but also as a weight function mapping subsurface conductivity into an apparent conductivity, the use of half-space sensitivity functions in approximate inversion approaches (imaging schemes) has been demonstrated in several pub-

lications (Gomez-Trevino, 1987a, 1987b, 2002; Pérez-Flores et al., 2001).

Wang et al. (2009) present an approach to borehole induction log inversion that reduces computation time considerably. The most important developments contributing to the speed-up of the inversion are the subdivision of the full-inversion problem into overlapping volumes based on the limited extent of the sensitivity function of the induction log (domain decomposition), and the use of an approximate method of finding the derivatives. Approximate derivatives are calculated based on the sensitivity function of a homogeneous half-space penetrated by a borehole calculated once at program start and subsequently used in the iterative inversion.

An approximation that appears quite often in the literature on sensitivity functions is one based on Biot-Savart's law. The electric field in the ground from the transmitter is calculated accurately, but the way the subsurface currents influence the Rx is found through a free-space approximation using Biot-Savart's law. This approach was used in Christensen (1995) in calculating approximate 1D vertical sensitivities for TEM data in an adaptive approach and extended for approximate 2D inversion in Christensen (1997) and Wolfram et al. (2003). The Biot-Savart approximation was also used in Reid et al. (2006) for improved footprint estimates.

In this paper, accurate sensitivity functions are derived, taking the full induction into account, and a numerical approach that is quite general is outlined. The sensitivity distribution for TEM systems varies significantly with the transmitter-receiver configuration, but only a limited number of configurations can be shown in a publication of this type. I have chosen to examine the central loop configuration, as a ground-based and an airborne system, and an airborne offset loop system. The principle character of most other configurations can be inferred from the properties of the two. Sensitivities for vertical- and horizontal-field components and for both impulse and step response will be investigated. Three-dimensional sensitivity distributions are visualized through appropriate cross sections together with images of the matching 2D and 1D sensitivity functions. Finally, a simple footprint measure is estimated for some of the sensitivities for which such a simplification can be justified.

THEORY

System configurations

In the following, I consider circular loop transmitters (Tx) and dipole receivers (Rx). Furthermore, I restrict the investigation to Tx/Rx oriented along the x -, y -, or z -axis in a standard right-hand Cartesian coordinate system with the z -axis pointing vertical down and the x -axis located at the earth surface in the vertical Tx-Rx plane, pointing in the direction of flight for airborne systems. In principle, there are nine different configurations to consider, but only a few are relevant for TEM systems. Almost all TEM systems use a horizontal Tx coil (vertical axis) because the response to this Tx type is much larger than to a horizontal axis coil. Considering 1D earth models, only z - or x -directed Rx dipoles will have a non-zero response to a z -directed Tx coil. I, therefore, limit my investigation to the situations with a circular Tx coil with axis along the z -axis and the Rx dipoles being z - and x -directed.

Earth model

For simplicity, I only consider a homogeneous half-space earth model. As will be seen, the structure of the sensitivity functions can be quite complicated even for this simple model. If conductivity contrasts are not too high, the structure of the half-space sensitivity function can be considered as a good approximation to that of a layered 1D model if the half-space conductivity is chosen equal to the apparent conductivity at the delay time considered (Boerner and Holladay, 1990).

Sensitivity functions

The sensitivity function is basically the derivative of a model response with regard to the subsurface conductivity. In three dimensions, it defines point sensitivities relating small changes in forward responses to small conductivity changes in infinitesimal earth volumes. For a given point in the earth, the 3D sensitivity basically reflects the potential resolution of the conductivity at this point: the higher the absolute value of the sensitivity, the better the potential resolution, and vice versa. The sensitivity function can attain positive and negative values, meaning that the response will increase or decrease, respectively, with increasing subsurface conductivity.

In the frequency-domain, the 3D sensitivity distribution S^{3D} is formally given as the dot product of the induced electric field strength from the transmitter \mathbf{E}_{Tx} , and the induced-electric field strength from the receiver, had it functioned as a transmitter, \mathbf{E}_{Rx} (McGillivray et al., 1994). Thus,

$$\begin{aligned} S^{3D}(\mathbf{r}, \mathbf{r}_{Tx}, \mathbf{r}_{Rx}, \omega) &= \mathbf{E}_{Tx}(\mathbf{r}, \mathbf{r}_{Tx}, \omega) \cdot \mathbf{E}_{Rx}(\mathbf{r}, \mathbf{r}_{Rx}, \omega) \\ &= E_{Tx}^x(\omega) \cdot E_{Rx}^x(\omega) + E_{Tx}^y(\omega) \cdot E_{Rx}^y(\omega) \\ &\quad + E_{Tx}^z(\omega) \cdot E_{Rx}^z(\omega), \end{aligned} \quad (1)$$

where \mathbf{r} is the position vector for any point in the half-space; \mathbf{r}_{Tx} and \mathbf{r}_{Rx} are position vectors for the Tx and Rx, respectively; x -, y -, z -axis are the direction of Cartesian coordinate system and ω is the angular frequency (see Figure 1). The sensitivity defined above is the induction sensitivity and the sensitivity for the magnetic field is obtained by integration, equivalent to division by $i\omega$ in the frequency domain (Tølbøll and Christensen, 2007).

Using the convolution theorem, the corresponding expression in the time domain is given as a convolution between the time-domain electric-field components (e.g., Hördt, 1998):

$$\begin{aligned} S^{3D}(\mathbf{r}, \mathbf{r}_{Tx}, \mathbf{r}_{Rx}, t) &= E_{Tx}^x(t) * E_{Rx}^x(t) \\ &\quad + E_{Tx}^y(t) * E_{Rx}^y(t) + E_{Tx}^z(t) * E_{Rx}^z(t). \end{aligned} \quad (2)$$

For the half-space model considered here and for a Tx above the surface, the subsurface electric-field will have only horizontal components, so

$$S^{3D}(\mathbf{r}, \mathbf{r}_{Tx}, \mathbf{r}_{Rx}, t) = E_{Tx}^x(t) * E_{Rx}^x(t) + E_{Tx}^y(t) * E_{Rx}^y(t). \quad (3)$$

By the same argument as above, the time-domain sensitivity defined in equation 3 is the impulse response sensitivity, i.e., the sensitivity

for the time derivative of the magnetic field, most often measured in an induction coil. The sensitivity of the step response, i.e., the magnetic field itself, is obtained by integrating the impulse sensitivity over time.

The definitions in equations 1 and 3 illustrate that the sensitivity distribution is basically a function of the electric-field distributions. The fundamental behavior of the electric field in the frequency domain inside a conductive half-space due to magnetic dipole transmitters is described by various authors (Kovacs et al., 1995; Beamish, 2003; Yin and Hodges, 2005; Tølbøll and Christensen, 2007) and shall not be described in further detail here. However, an important scaling property is that, for a given Tx-Rx geometry, the induced electrical field depends only on transmitter frequency and half-space conductivity and remains unchanged for a constant frequency-conductivity product $\omega\sigma$. It is consequently possible to analyze its general behavior as a function of the Tx-Rx configuration and the $\omega\sigma$ parameter, and the same applies to the sensitivity distribution. This scaling property is noted by Boerner and Holladay (1990) and is used to express the sensitivity function for a layered earth as approximately equal to the half-space sensitivity function for a half-space conductivity equal to the apparent conductivity of the measurement. In the time domain, this means that, for a given Tx-Rx geometry, the sensitivity function scales in the ratio between time and half-space conductivity t/σ , and the same adaptive approach can be used. The layered half-space sensitivity function is approximately the same as the half-space function for a conductivity equal to the apparent conductivity of the measurement.

Numerical implementation

The practical calculations of the 3D sensitivity distribution poses a series of challenges in terms of accuracy and computational speed. The formulas for the frequency-domain subsurface electric field in a homogeneous half-space are given in Appendix A. The time-domain sensitivity could be found by calculating the frequency-domain electric fields for a series of frequencies and wavenumbers, multiplying the Tx and Rx contributions as shown in equation 1, and then performing a Fourier transformation from frequency to time followed by a Hankel transform from wavenumber to space.

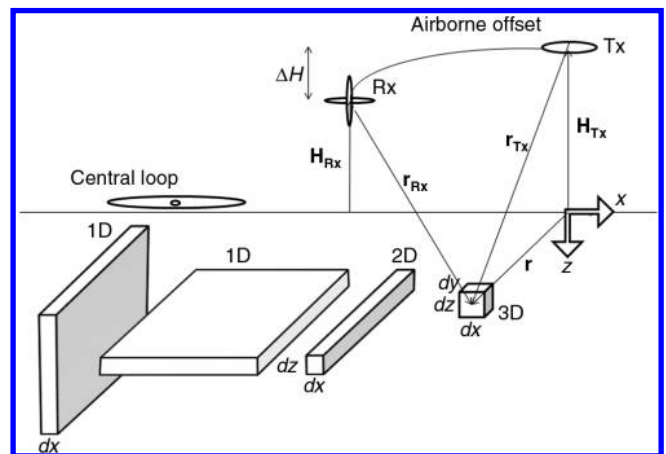


Figure 1. The sketch illustrates a central loop configuration and an airborne offset loop configuration together with 3D, 2D, and 1D model elements for vertical and horizontal sensitivity functions.

This approach was investigated, implementing the Fourier transform with cosine and sine filters using the fast Hankel transform theory (Christensen, 1990). However, the aim is to calculate sensitivity functions accurately for a wide interval of delay times, and it turned out to be difficult to obtain sufficient accuracy at very early times with the above approach. This can be attributed to the highly oscillatory nature of the frequency-domain electric fields at high frequencies.

Instead, I have used the fact that an analytic expression exists for the electric field in the time/wavenumber domain (see Appendix A), so only a Hankel transform from wavenumber to space domain is necessary to calculate the field in time and space. This, of course, drastically reduces computation time, and the numerically challenging transformation from frequency (or Laplace) to time domain is avoided. The sensitivity function is then calculated in the time domain as a convolution between the Tx field and the Rx field. This, however, poses another serious challenge. The character of the time-domain field at a point in a homogeneous half-space is illustrated in Figure 2. It is seen that for times smaller than the diffusion time pertaining to the position and half-space conductivity, the response is practically zero. Then the amplitude rises extremely abruptly over a time interval of only fractions of a microsecond and reaches a maximum, after which the amplitude falls off slowly and the function becomes very smooth. A discrete sampling of the time-domain field must be able to capture this behavior, and it is therefore necessary to sample the function very densely with a sampling interval of the order of 1–10 ns. On the other hand, to be able to find the sensitivity function at very late times, the field amplitude must be sampled to very late times of the order of 10 s. An equidistant sampling will therefore contain up to 10^8 – 10^{10} samples and a discrete convolution that has to be carried out for every single sample in the 3D volume becomes prohibitively time consuming. Various methods of solving this basic challenge have been suggested in the literature (e.g., Hördt, 1998). In this paper, the problem is solved by sampling the electric field logarithmically so that the density is appropriate at early times whereas the sampling distance becomes

large at late times where the function is smooth. The convolution is then implemented as a numerical integration using local splines by resampling the Tx and Rx fields to have coincident samples (see Appendix B).

2D and 1D sensitivity functions

Sensitivity distributions of lower dimensions are found by numerically integrating the 3D sensitivity distribution along relevant axes, and I shall consider 2D and 1D sensitivities. The 2D sensitivity function relates changes in the response to conductivity changes of a 2D model element, i.e., a cylinder with infinite extent in the y -direction and infinitesimal cross section. The horizontal 1D sensitivity reflects the sensitivity of the TEM system to a vertical, infinite thin sheet oriented perpendicular to the x -axis, whereas the vertical 1D sensitivity describes the sensitivity to a horizontal thin sheet at the depth z . The 3D, 2D, and 1D model elements are illustrated in Figure 1.

The 3D sensitivity functions considered here are symmetric around the plane $y = 0$ and this is of course used, see equation 4. To keep computation time at a minimum without compromising accuracy, the sampling along the integration axes is done using a hyperbolic sine scheme, meaning that the sensitivity functions are sampled equidistantly and densely for small distances with the sampling distance increasing away from the center of the system; see equation 4. The sampling distance close to the axis is chosen sufficiently small and the integration area sufficiently large to ensure a reliable result:

$$S^{2D}(x, z, t) = \int_{-\infty}^{\infty} S^{3D}(x, y, z, t) dy = 2 \int_0^{\infty} S^{3D}(x, y, z, t) dy,$$

$$S^{2D}(x, z, t) = 2 \int_0^{\infty} S^{3D}(x, \sinh(v), z, t) \cosh(v) dv. \quad (4)$$

By integrating S^{2D} over x , we obtain the vertical 1D sensitivity function as a function of depth, z . The x -axis is split into two at $x = x_0$, where x_0 is the midpoint between Tx and Rx, and the sinh sampling

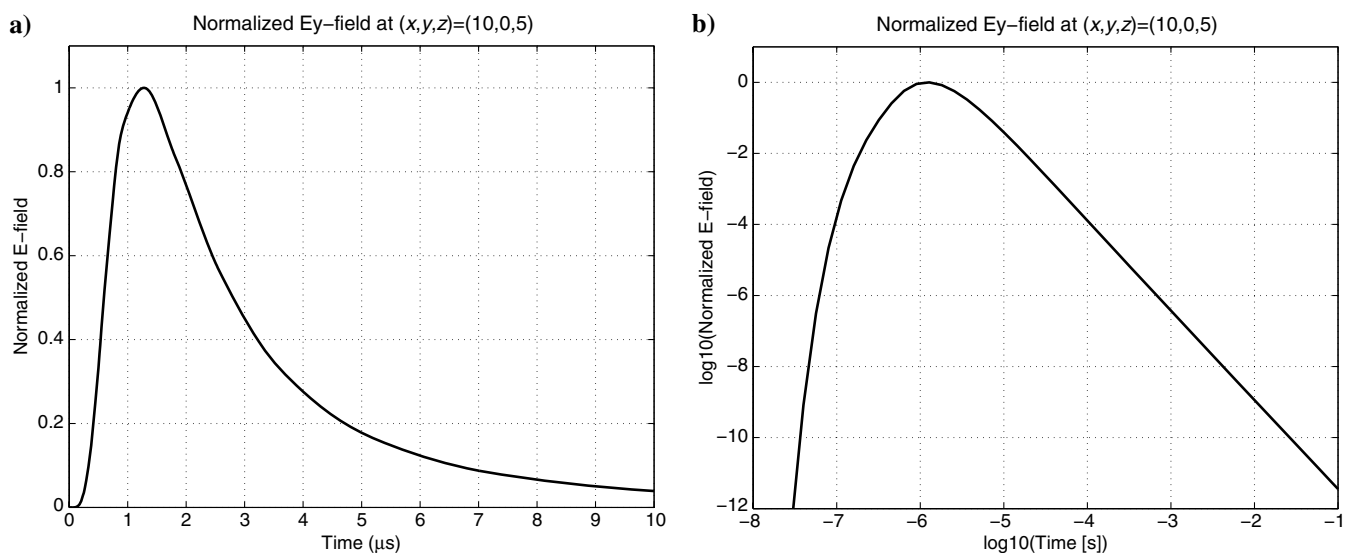


Figure 2. The electric field at $\mathbf{r} = (10, 0, 5)$ as a function of time from a vertical-magnetic-dipole source at the surface of a homogeneous half-space. (a) Linear plot and (b) logarithmic plot.

is implemented from x_0 toward $\pm\infty$. All numerical integrations are performed by integrating over 11 points at a time using the closed 11-point formula of Abramowitz and Stegun (1972), equation 25.4.20) and then adding the values together. The summation is truncated when the last term is smaller than a predefined relative truncation error:

$$\begin{aligned} S^{1Dz}(z, t) &= 2 \int_{-\infty}^{\infty} dx \int_0^{\infty} S^{3D}(x, y, z, t) dy, \\ S^{1Dz}(z, t) &= 2 \int_{-\infty}^{\infty} dx \int_0^{\infty} S^{3D}(x, \sinh(v), z, t) \cosh(v) dv, \\ S^{1Dz}(z, t) &= 2 \int_{-\infty}^{x_0} \cosh(u) du \int_0^{\infty} S^{3D}(\sinh(u), \sinh(v), z, t) \cosh(v) dv \\ &\quad + 2 \int_{x_0}^{\infty} \cosh(u) du \int_0^{\infty} S^{3D}(\sinh(u), \sinh(v), z, t) \cosh(v) dv. \end{aligned} \quad (5)$$

Beside the vertical 1D sensitivity function defined in equation 5, a horizontal 1D sensitivity function is defined in equation 6:

$$\begin{aligned} S^{1Dx}(x, t) &= 2 \int_0^{\infty} dz \int_0^{\infty} S^{3D}(x, y, z, t) dy, \\ S^{1Dx}(x, t) &= 2 \int_0^{\infty} dz \int_0^{\infty} S^{3D}(x, \sinh(v), z, t) \cosh(v) dv, \\ S^{1Dx}(x, t) &= 2 \int_0^{\infty} \cosh(u) du \int_0^{\infty} S^{3D}(x, \sinh(v), \sinh(u), t) \cosh(v) dv. \end{aligned} \quad (6)$$

Computation times

The figures in this paper in the parallel and perpendicular projections are made from a matrix of 41 samples in depth and 141 samples in the lateral direction; the images in the plane projection has 141×141 samples.

Computation time for the electrical fields from the Tx and Rx is ~ 10 ms for every depth level involved in the computations, and interpolation and integration takes up most of the computation time. For the integration in the y -direction, 70 points are used along the y -axis, for the integration on the x -direction 140 points are used, and for the z -integration 50 points are used. The computational cost of the numerical integration itself is insignificant compared with the cost of interpolation, which is ~ 0.5 ms per point on average. A single image in the resolution used in this paper thus takes ~ 10 s in the plane projection, a parallel view takes ~ 3 s, and a 2D or 1D sensitivity function takes ~ 200 s on a single thread on a 2 GHz CPU.

THE SENSITIVITY FUNCTIONS

In the following, I consider sensitivity functions for two typical TEM configurations: a ground-based and an airborne central loop configuration and an airborne offset loop configuration used by many fixed wing systems. See Figure 1 for a sketch of the two configurations. The space allotted to a journal paper does not permit more configurations to be considered, but the sensitivity functions pertaining to other configurations can, with a bit of good will, be inferred from these two examples.

A word about plotting conventions for the figures of sensitivity functions: As a function of delay time, transient electromagnetic fields cover a huge dynamic range, and this property is even more pronounced for sensitivity functions being convolutions between electric fields. In each frame of the following figures, the amplitude is, therefore, normalized with the maximum of the absolute value at the pertinent delay time. To avoid wobbly contours due to a limited computational accuracy, the zero contours are implemented as contours of the value ± 0.001 .

Diffusion of current density and sensitivity functions

To illustrate some basic concepts, Figure 3 shows four plots: one of the current density, one of the Biot-Savart-type step response sensitivity function, and one of the true step response sensitivity function — all plots for a ground-based, ideal coincident vertical-magnetic-dipole configuration. The fourth plot is for a ground-based central loop configuration with a Tx radius of 50 m. All four plots show frames for the delay times of 20, 80, and 320 μ s.

For any delay time t , the current density has the largest and the true sensitivity function the smallest vertical extent, whereas the Biot-Savart-type sensitivity function lies in between. This means that if one uses the spatial extent of the current density to estimate penetration depth — as has been done in the past — it will be severely overestimated. Also, the Biot-Savart approximation to the sensitivity function will overestimate the vertical extent of the true sensitivity function (Reid et al., 2006), and if used in an imaging procedure to find an approximate subsurface conductivity structure from measured data, a scaling factor must be introduced to avoid underestimating model depths (Christensen, 1995).

All three plots for the coincident vertical-magnetic-dipole configuration preserve their shape for increasing delay times t , their spatial extent being proportional to diffusion length, i.e., $\propto \sqrt{t}$. For the true sensitivity function, the sensitivity is small in an earth volume within a cone with a vertical axis centered at the center of the configuration. Furthermore, at all delay times, the maximum of the sensitivity is at the surface, meaning that maximum sensitivity does not coincide with the maximum of the current density. The latter observation disqualifies another popular misconception, namely that the maximum sensitivity diffuses into the ground with increasing delay time. Rather one should think of the sensitivity at a time t_2 , as a stretching of the sensitivity function at the time t_1 with a factor of $\sqrt{t_2/t_1}$. The shape is preserved and the maximum sensitivity stays at the surface, but the contribution from depths greater than a certain limit becomes relatively larger.

The true sensitivity function for a central loop configuration with a Tx radius of 50 m illustrates that, for increasing Tx loop radius, the width of the sensitivity function increases for early times, whereas for later times, the sensitivity function becomes less dependent on the Tx radius. The value of the sensitivity function is also more evenly distributed than in the coincident dipole case. However, the depth extent is only weakly dependent on the Tx loop radius.

The effect of transmitter height

In Figure 4, the 3D step response sensitivity function for a central loop system is shown for several heights for a constant delay time of 10 μ s and a half-space conductivity of 0.05 S/m. The figure illustrates that the lateral extent of the sensitivity function increases with

height, whereas the vertical extent is fairly much the same for all heights.

Taking the 10% contour as a measure of the width of the sensitivity function, the width as a function of height is plotted in Figure 5. For the height interval shown here, the width increases approximately proportional to the Tx elevation.

The central loop configuration

In Figures 6, 7, 8, and 9, the sensitivity distributions are illustrated by a horizontal section through the 3D sensitivity at the surface (the plane $z = 0$), a vertical section through the 3D sensitivity through the line connecting the Tx and Rx (the plane $y = 0$), the same vertical section through the 2D sensitivity, and a plot of the horizontal 1D sensitivity function. Impulse and step response sensitivities are shown. The sensitivity functions are plotted for only one delay time.

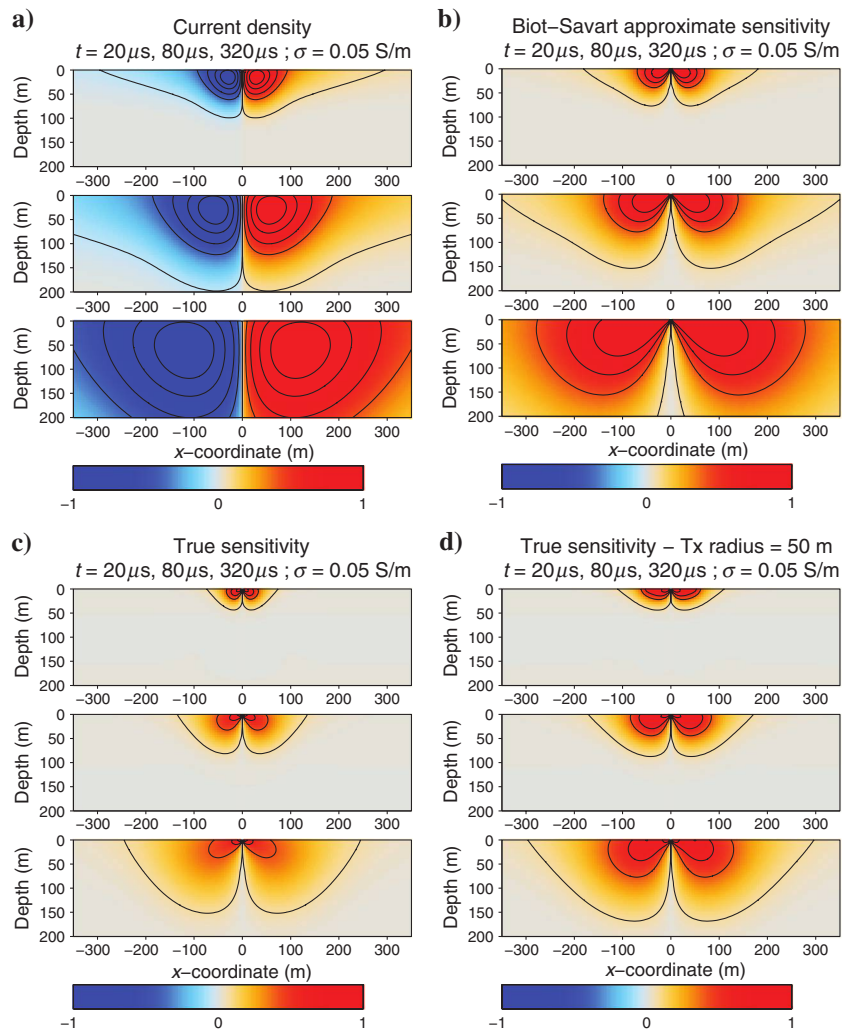
First, let us consider the simple configuration of a ground-based central loop configuration with a transmitter radius of 20 m. Figure 6 illustrates the 3D, 2D, and horizontal 1D behavior of a ground-based central loop configuration for the z -component for the step and the impulse response.

Comparing the 3D and 2D sensitivity functions in Figure 6, it is seen that the 2D sensitivity function is overall smoother and later-

ally slightly wider. The 1D lateral sensitivity function has its maximum at the center of the configuration, except for a small local minimum at the center. The sensitivity functions for the impulse response display an additional zero crossing. This is to be expected, considering that the impulse response is the time derivative of the step response. The effective width of the sensitivity function is comparable to that of the step response; the positive central area shrinks a bit to make room for the negative side lobes.

Though an x -directed receiver coil at the center of a circular loop will have a zero response over a 1D earth, the 3D sensitivity distribution has positive and negative values, see Figure 7. However, the integral of the 3D sensitivity function over x and y for any depth z will, of course, be zero. The sensitivity functions for the step response of the x -component is considerably more complicated than that of the z -component. It is symmetric about the plane $x = 0$ and has a positive and a negative volume of high amplitude surrounded by volumes with negative and positive values of smaller amplitudes. This character can be seen in both the 3D, 2D, and 1D sensitivity functions (Figure 7). The 1D lateral sensitivity function shows that, essentially, the x -sensitivity effectuates a lateral differentiation of the conductivity structure, meaning that the x -response is more sensitive to lateral changes in conductivity than the z -response. For a central loop configuration, a nonzero x -component of the response

Figure 3. (a) Vertical section through the current density for a ground-based coincident vertical-magnetic-dipole configuration. The contour lines are for the (scaled) values of 0, 0.1, 0.25, 0.50, and 0.75. (b) Vertical section through the step response true sensitivity function for a ground-based coincident vertical-magnetic-dipole configuration. The contour lines are for the (scaled) values of 0, 0.1, 0.25, and 0.50. (c) Vertical section through the step response true sensitivity function for a ground-based coincident vertical-magnetic-dipole configuration 0.1, 0.25, and 0.50. (d) Vertical section through the step response true sensitivity function for a central loop configuration with Tx radius of 50 m. The contour lines are for the (scaled) values of 0, 0.1, 0.25, and 0.50.



indicates that there are lateral gradients in the conductivity distribution and that the earth is not 1D. In the case of data being inverted with a 1D model, a nonzero x -component is only of qualitative use; in 2D and 3D inversion, the x -component can be included together with the z -component to improve resolution.

In the same way as previously seen for the z -component, the impulse response sensitivity function for the x -component has additional side lobes of alternating sign, thereby increasing the effective order of lateral differentiation while preserving the overall lateral dimensions.

The 1D vertical sensitivity functions will be presented after the next section.

An airborne offset loop configuration

The offset loop configuration is used by several airborne systems, e.g., TEMPEST (Lane et al., 2000) and GEOTEM (Pedersen and Thompson, 1991). I shall consider a generic configuration at the delay time $200 \mu\text{s}$ with a circular Tx loop with a radius of 10 m at an elevation of $H_{Tx} = 100 \text{ m}$ and z - and x -directed Rx dipoles

at an elevation of $H_{Rx} = 80 \text{ m}$ trailing 100 m behind the Tx loop. The configuration is sketched in Figure 1.

In Figures 8 and 9, plots corresponding to Figures 4 and 5 are shown for the offset configuration; i.e., Figure 8 shows step and impulse response sensitivity functions for the z -component and Figure 9 the corresponding functions for the x -component. In the plot frames of the two figures, the Tx loop is placed at $x = 50$, whereas the Rx dipoles are placed at $x = -50$. Notice that the x -coordinate interval is twice as wide as in Figures 6 and 7. This is necessary because the configuration is offset and airborne, and the vertical exaggeration is a factor of two.

Looking at the z -component, the first thing to be noticed is that the sensitivity is negative within a vertical cylinder with the Tx-Rx line as diameter. The subsurface electric fields from the Tx and Rx are circular, centered on the Tx and Rx, respectively, and the angle between the field vectors is numerically larger than $\pi/2$, making the dot product negative. In the 2D sensitivity function, the negative zone persists at early times, but at the delay time of $200 \mu\text{s}$ considered here, it has disappeared. The 1D lateral sensitivity function displays the typical M-shape with a pronounced central minimum. This shape explains the typical, well-known M-shaped anomaly measured over a discrete vertical conductor. The impulse sensitivity function for the offset configuration has one more zero crossing in the vertical direction and the 1D lateral sensitivity function has small negative side lobes. As for the central loop configuration, the overall extent of the impulse sensitivity function is approximately the same as for the step response.

The sensitivity functions for the x -component are more complicated than any of the previous ones. The step response sensitivity function has a central positive volume centered below the Rx. Embedded in the positive sensitivity is a volume of a quite complex shape with negative sensitivity in front of the Tx. The sensitivity function is also negative behind the positive volume. This structure persists in the 2D sensitivity function. The lateral 1D sensitivity function is nonsymmetrical with a positive and a negative lobe.

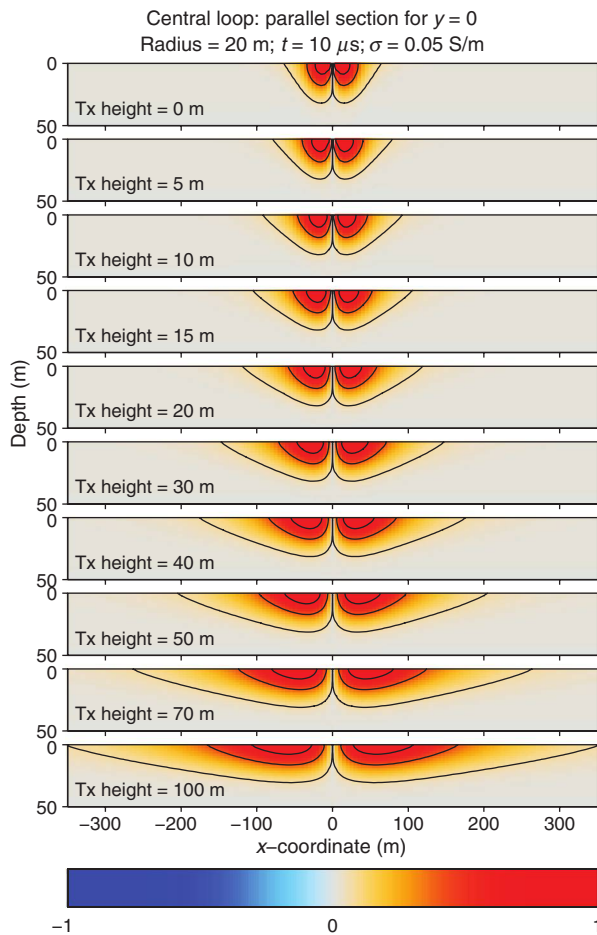


Figure 4. Vertical section through the 3D sensitivity function for the step response of the z -component of a central loop configuration as a function of Tx height. The contour lines are for the (scaled) values of 0, 0.1, and 0.5. Radius of the circular transmitter loop is 20 m, delay time is $10 \mu\text{s}$, and half-space conductivity is 0.05 S/m .

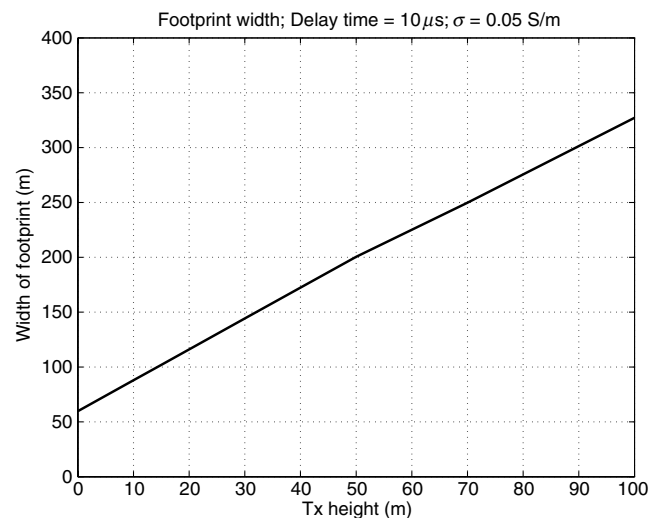


Figure 5. The width of the 3D sensitivity function for the step response of the z -component of a central loop configuration as a function of Tx height. Radius of the circular transmitter loop is 20 m, delay time is $10 \mu\text{s}$, and half-space conductivity is 0.05 S/m .

Figure 6. The 3D, 2D, and horizontal 1D sensitivity functions for the z -component of a ground-based central loop configuration. Tx and Rx positions are in (0,0). (a) Step response and (b) impulse response. The sensitivity functions are scaled to have a maximum absolute value of one and the contour lines are for the (scaled) values of 0, 0.2, 0.4, and 0.6. Radius of the circular transmitter loop is 20 m, delay time is 200 μ s, and half-space conductivity is 0.05 S/m. The scaling constants are given in the plot frames as F0.

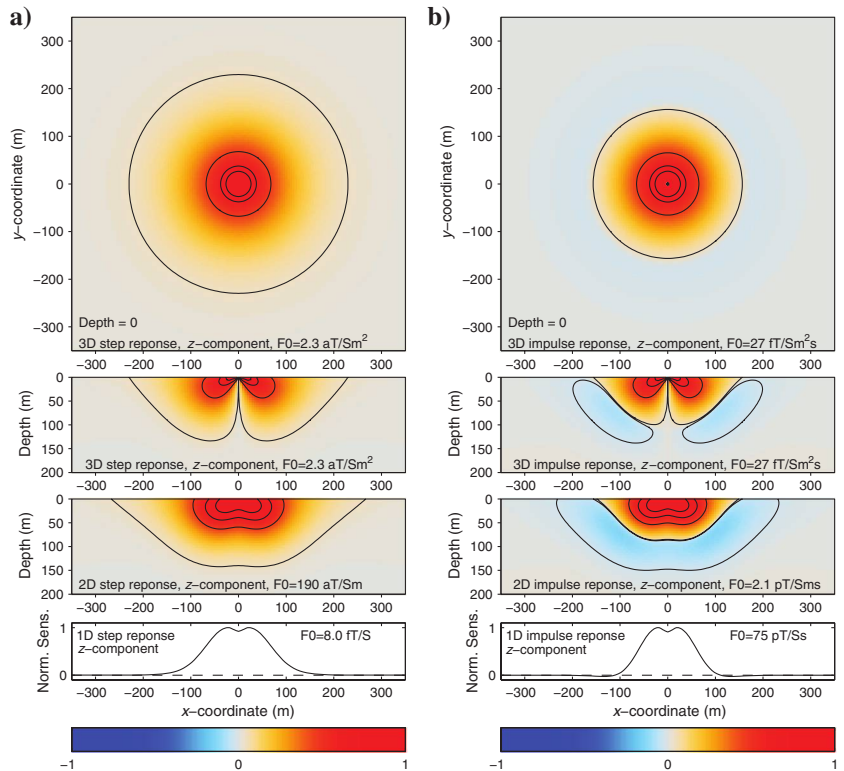
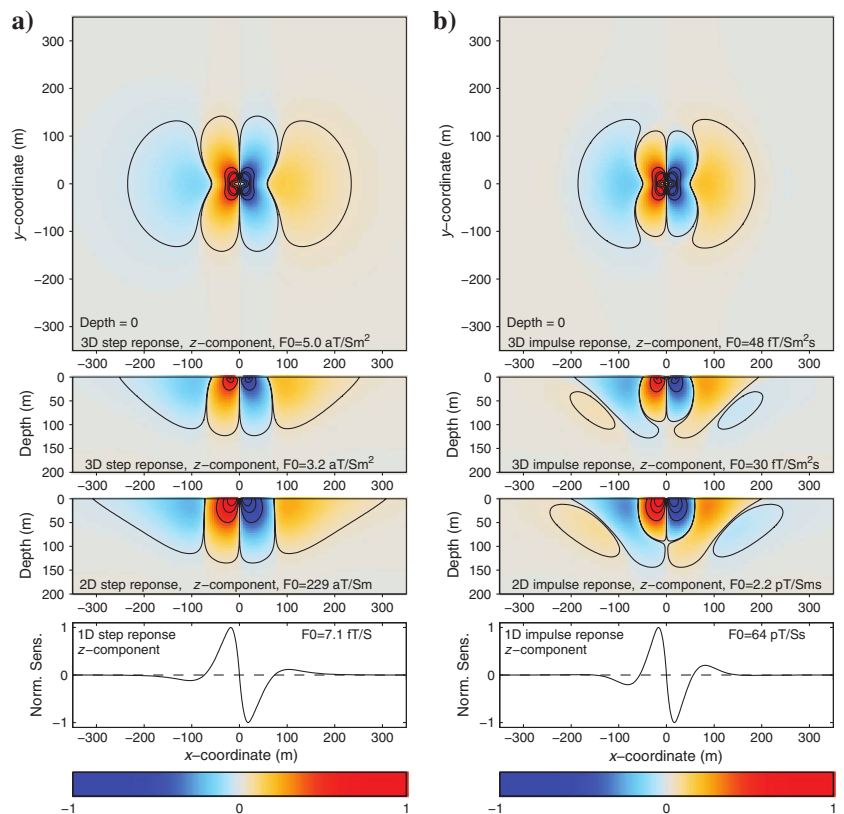


Figure 7. The 3D, 2D, and horizontal 1D sensitivity functions for the x -component of a ground-based central loop configuration. Tx and Rx positions are in (0,0). (a) Step response and (b) impulse response. The sensitivity functions are scaled to have a maximum absolute value of one and the contour lines are for the (scaled) values of 0, 0.2, 0.4, and 0.6. The radius of the circular transmitter loop is 20 m, delay time is 200 μ s, and half-space conductivity is 0.05 S/m. The scaling constants are given in the plot frames as F0.



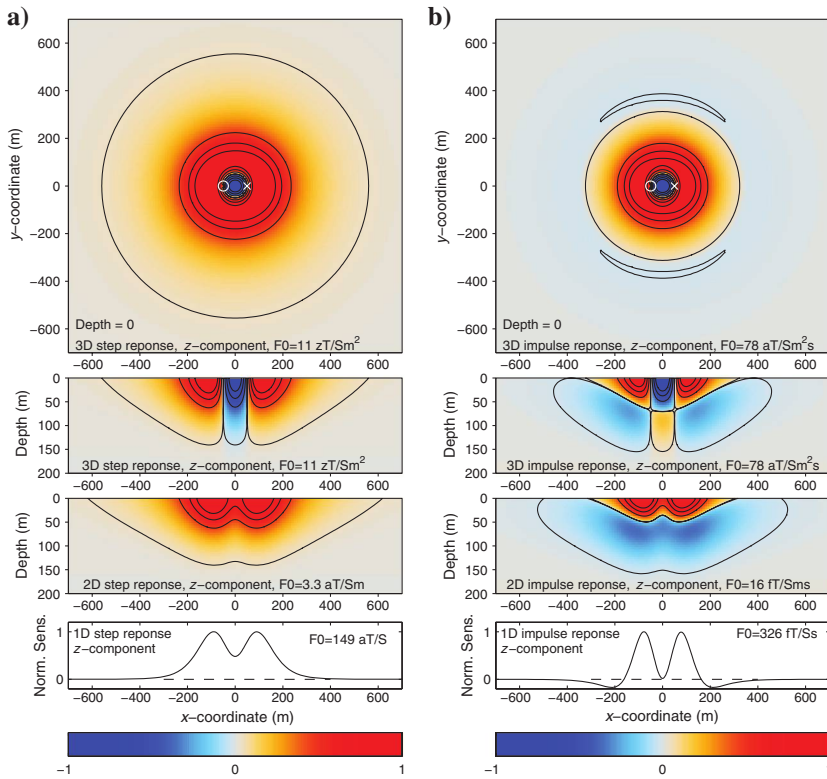


Figure 8. The 3D, 2D, and horizontal 1D sensitivity functions for the z -component of an airborne offset loop configuration with a circular Tx loop with a radius of 10 m at an elevation of 100 m and Rx dipoles trailing 100 m behind and 20 m below the Tx loop. The Tx and Rx positions are indicated with a white cross and circle, respectively. (a) Step response and (b) impulse response. The sensitivity functions are scaled to have a maximum absolute value of one and the contour lines are for the (scaled) values of 0, 0.2, 0.4, and 0.6. The delay time is 200 μ s and half-space conductivity is 0.05 S/m. The scaling constants are given in the plot frames as F0.

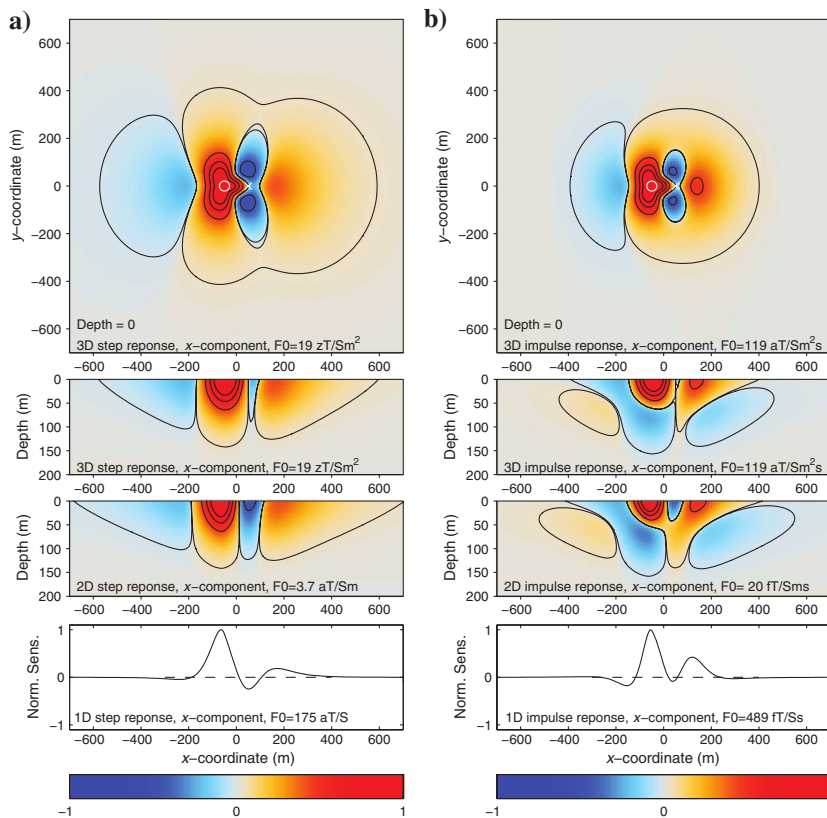


Figure 9. The 3D, 2D, and horizontal 1D sensitivity functions for the x -component of an airborne offset loop configuration with a circular Tx loop with a radius of 10 m at an elevation of 100 m and Rx dipoles trailing 100 m behind and 20 m below the Tx loop. The Tx and Rx positions are indicated with a white cross and circle, respectively. (a) Step response and (b) impulse response. The sensitivity functions are scaled to have a maximum absolute value of one and the contour lines are for the (scaled) values of 0, 0.2, 0.4, and 0.6. The delay time is 200 μ s and half-space conductivity is 0.05 S/m. The scaling constants are given in the plot frames as F0.

As seen before, the impulse sensitivity functions for the x -component have one more zero crossing in the vertical direction. They are the most complicated ones considered so far, and the negative side lobes of the 1D lateral sensitivity function are more pronounced.

The complicated shape with positive and negative values of the x -component sensitivity function explains why it is often quite difficult to include x -component data together with z -component data in 1D inversion of TEM data; for an increasing degree of multidimensionality of the subsurface conductivity distribution, the x -component leaves the domain where a 1D assumption is viable much sooner than the z -component. The challenges and the usefulness of including the x -component in the 1D inversion of TEM data are analyzed in Kirkegaard et al. (2012), whereas Smith and Keating (1996) present a case for the usefulness of x -component data in looking for discrete conductors due to its sensitivity to lateral conductivity changes in the subsurface.

The effect of waveform

Above, the sensitivity functions for the ideal step and impulse responses have been illustrated, i.e., the magnetic field response B and the derivative of the magnetic field response dB/dt from a current that has been on forever and then turned off infinitely fast at time zero. In real life, the rate of change of the Tx current is of course finite and the measured responses are found as convolutions between the ideal response and the time derivative of the Tx current.

For the simple case of a linear turnoff ramp, the measured off-time response in an induction coil dB/dt can be found as

$$\frac{dB_{\text{meas}}}{dt} = \frac{B(t - t_{\text{off}}) - B(t)}{t_{\text{off}}}, \quad (7)$$

where t is measured from the start of the ramp and t_{off} is the ramp time. For t close to t_{off} , $t = t_{\text{off}} + \Delta t$, we have

$$\begin{aligned} \frac{dB_{\text{meas}}}{dt} &= \frac{B(t_{\text{off}} + \Delta t - t_{\text{off}}) - B(t_{\text{off}} + \Delta t)}{t_{\text{off}}} \\ &= \frac{B(\Delta t) - B(t_{\text{off}} + \Delta t)}{t_{\text{off}}}, \\ \frac{dB_{\text{meas}}}{dt} &\approx \frac{B(\Delta t)}{t_{\text{off}}} \end{aligned} \quad (8)$$

because $B(\Delta t) \gg B(t_{\text{off}} + \Delta t)$. At very early times in the off-time, the dB/dt response — and thereby also the sensitivity function — resembles that of a step response scaled with t_{off} . As delay time increases, the response will smoothly change from being B -like to becoming more dB/dt -like; at late times $t \gg t_{\text{off}}$, the response — and thereby also the sensitivity function — is essentially that of an ideal impulse response.

If a linear turn-on ramp of the current is included, the measured response becomes

$$\frac{dB_{\text{meas}}}{dt} = \frac{B(t - t_{\text{off}}) - B(t)}{t_{\text{off}}} - \frac{B(t + t_w) - B(t + t_w - t_{\text{on}})}{t_{\text{on}}}, \quad (9)$$

where t_w is the width of the current waveform from start of turn-on to start of turnoff and t_{on} is the length of the turn-on ramp. If $t_{\text{on}} \ll t_w$, we have for off-time measurements

$$\frac{dB_{\text{meas}}}{dt} \approx \frac{B(t - t_{\text{off}}) - B(t)}{t_{\text{off}}} - \frac{dB}{dt}(t + t_w). \quad (10)$$

At very early times in the off time, $(t + t_w) \gg t$ and the last term vanishes so the sensitivity to the length of the ramp is very small. At late times, where $(t + t_w)$ is of the same order of magnitude as t , the measured response can be written,

$$\frac{dB_{\text{meas}}}{dt} \approx \frac{dB}{dt}(t) - \frac{dB}{dt}(t + t_w). \quad (11)$$

This is the well-known so-called run-on effect, and the sensitivity function will therefore be the difference between the two impulse response sensitivity functions of which the first term is the dominating one.

Issues involved in defining a footprint

For simple all-positive sensitivity functions like the ones considered in Figure 4, it is straightforward to define a footprint, but the sometimes highly complex nature of the sensitivity distributions poses some challenges with regard to a reasonable definition of the footprint. As an example, consider the definition of the footprint as the interval where the value of the sensitivity function is above a certain limit, e.g., 10%. When the sensitivity function has zero crossings and negative subvolumes this definition become ambiguous. Defining the footprint in terms of the lateral area within which the integral of the sensitivity is above a certain limit suffers the same difficulties. With positive and negative values, the integral is not necessarily a monotoneous function of integration area and also this definition becomes ambiguous. Under all circumstances, the full sensitivity function offers much more information than can be expressed through a footprint measure.

The 1D vertical sensitivity functions

In Figure 10, the 1D vertical sensitivity function of a ground-based central loop configuration is shown for the three delay times of 10, 100, and 1000 μs . The figure illustrates the scaling of the 1D sensitivity function. The sensitivity function for the three delay times have similar shapes in a log-log plot, but the surface amplitude decreases and the depth extent increases with increasing delay time.

In Figure 11, the 1D vertical sensitivity functions are shown for the configurations considered above to demonstrate similarities and differences. All sensitivity functions have been normalized to have a maximum absolute value of unity. It is evident in Figures 6–9 that the vertical extent of the sensitivity functions is rather similar for all configurations, and this is confirmed in Figure 11. Considering the very different 3D sensitivity distributions, it is surprising that the 1D vertical sensitivity functions should be that similar for the step response of the ground-based central loop and the airborne offset loop configurations.

Comparing the z -component step and impulse sensitivity functions, it is seen that the impulse sensitivity functions have a negative lobe at depth, small for the ground-based central loop

configuration, but much more pronounced for the airborne offset configuration. This explains why impulse response apparent resistivity curves display a small minimum before ascending to higher values, and vice versa. It is also seen that the step response 1D vertical sensitivity functions for the x -component for the offset configuration are quite similar to the ones for the z -component, a surprising result considering the evident differences in the 3D sensitivity distributions.

The fact that the 1D vertical sensitivity functions for the step responses do not seem to depend much on whether the configuration is ground based or airborne or whether one considers the z - or the x -component means that — theoretically, in principle — the subsurface conductivity is sensed and weighted in the same way in 1D inversion. However, the practically obtainable resolution and penetration depth for transient systems depends on many different factors. A comprehensive discussion is complicated and not the focus of this paper. However, I will mention a few of the main points related to the sensitivity functions described here.

It is well known that signal-to-noise properties and uncertainties of the configuration parameters such as Tx height or Tx-Rx distance differ widely for different systems. Both will directly or indirectly influence the obtainable vertical resolution, which can therefore be very different for different actual existing systems. An airborne system will have lower signal strength than a ground-based system, other system parameters kept constant, and it will be lower the higher the survey elevation, meaning that the signal-to-noise ratio (S/N) will decrease with height. Also, the signal strength of the x -component is most often smaller than that of the z -component, and the ambient noise is typically 5–10 times higher (McCracken et al., 1986; Spies, 1988; Nyboe and Sørensen, 2012), again meaning that the S/N will be inferior. Likewise, the uncertainty of the configuration parameters such as Tx height or Tx-Rx distance for, e.g., a fixed-wing airborne system with a trailing bird is considerably higher than the corresponding parameters of a rigid helicopter borne system. All these issues must be taken

into account when assessing the resolution properties of actual TEM instrumentation.

Half-space sensitivity functions for calculation of approximate derivatives

The sensitivity function, being the derivative of the response with regard to changes in conductivity within a model element, can be used in an approximate linear mapping, a Born approximation, of anomalous conductivity into changes in measured response, e.g., for the purpose of answering questions of detectability. With the computational approach of this paper, the sensitivity functions are readily available. However, considering the limited accuracy of the Born approximation for nonlinear problems, such as the TEM method, and the fact that accurate 2D and 3D responses can be obtained quite rapidly with modern computer programs, the most important role of the sensitivity function is in the immediate visual assessment of the distribution of sensitivity for a given method and thereby an initial qualitative assessment of the resolution capabilities.

A very important role for the sensitivity functions — of more practical value — is to provide approximate derivatives in a quantitative inversion. Approximate derivatives will quite often serve just as well as more accurate ones in the inversion with no loss of convergence (Boerner and Holladay, 1990), and calculating the derivatives from the half-space sensitivity functions is considerably faster, thus speeding up the inversion process. An example shall be given here of using the 1D sensitivity function to compute the derivatives in a 1D inversion of TEM data.

Figure 12a shows the derivatives of the step response with regard to layer conductivity for five different multilayer models: the reference model is a homogeneous half-space with a conductivity of 0.02 S/m; and in the other four models, the conductivity of the layer at 36–44-m depth is perturbed to become 0.03, 0.04, 0.01, and 0.0001 S/m. The configuration is an airborne central loop configuration at a height of 30 m with a Tx radius of 10 m and the delay

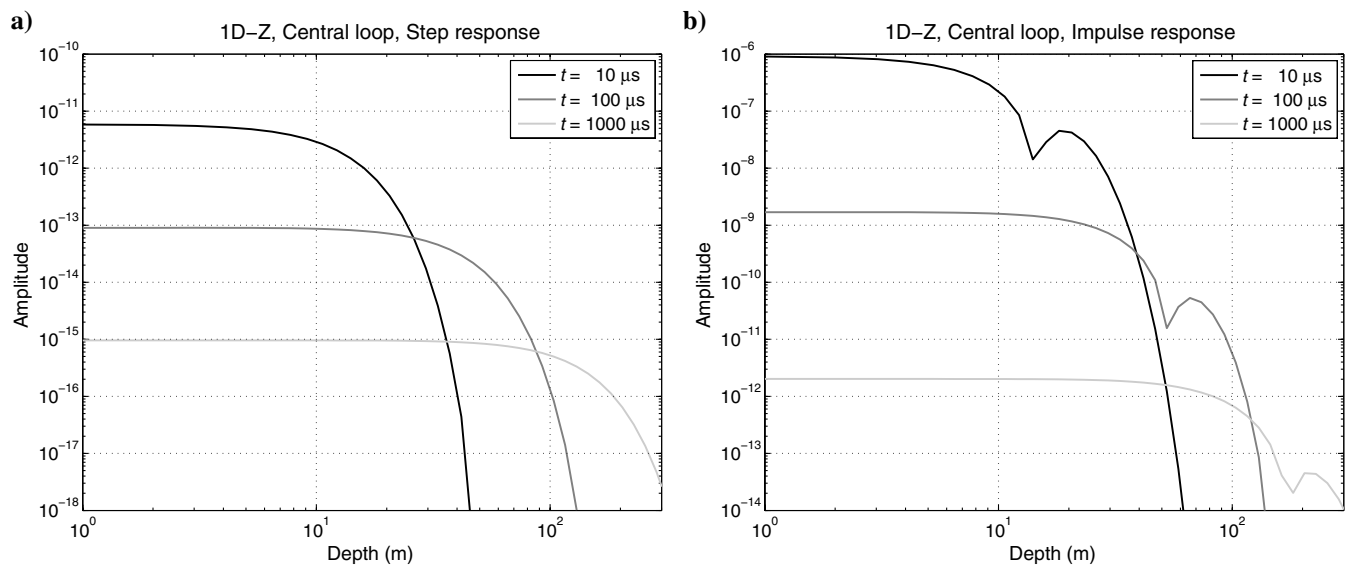


Figure 10. The vertical 1D sensitivity functions of a ground-based central loop configuration for the three delay times of 10, 100, and 1000 μs for (a) the step response and (b) the impulse response. The cusps of the latter indicate sign changes. The radius of the circular transmitter loop is 20 m, and half-space conductivity is 0.05 S/m.

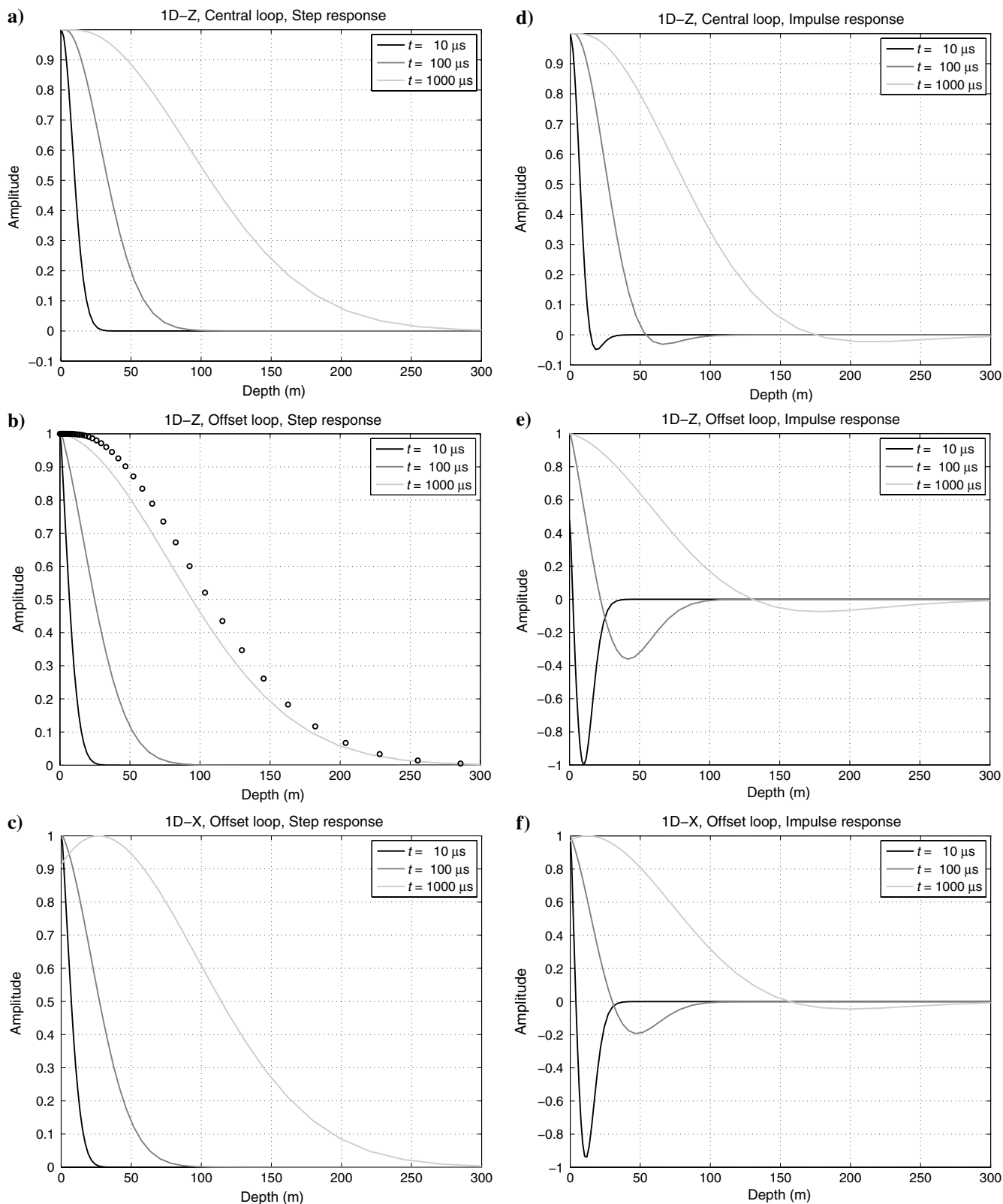


Figure 11. Normalized vertical 1D sensitivity functions for the three delay times of 10, 100, and 1000 μs . Left column is step response and right column impulse response sensitivity functions. (a and d) The z -component of the ground-based central loop configuration with a Tx radius of 20 m, (b and e) z -component of the airborne offset loop configuration. The offset loop configuration has a circular Tx loop with a radius of 10 m at an elevation of 100 m and Rx dipoles trailing 100 m behind and 20 m below the Tx loop. The red stars in the step response plot are for the central loop configuration for a delay time of 1000 μs for comparison, and (c and f) x -component of the airborne offset loop configuration.

time is 160 μs . The effect of the anomalous conductivity in the perturbed layer is clearly seen. Scaling the derivative in the perturbed layer, we arrive at Figure 12b. It is seen that the sensitivity functions are quite similar, but also slightly different: the ones pertaining to an increase of conductivity in the perturbed layer are higher at early times and vice versa. This is due to the fact that the electric field in the subsurface is influenced by the perturbed conductivity because, at a delay time of 160 μs , the sensitivity function encompasses the perturbed layer. Plotted in the same frame is the 1D sensitivity function calculated with the program presented in this paper and averaged over the model layers. It is seen that it is very similar to the derivative function for the half-space model with only very minor deviations close to the surface, most likely due to

numerical inaccuracies in the integration of the 3D sensitivity function. It is also clear that it will serve as a good approximation to the (scaled) derivatives for all five models.

The fact that the derivatives, to a first approximation, only vary moderately with varying subsurface conductivity, reflects that the electric field varies only moderately with the conductivity structure in a 1D earth, and that the current density is proportional to the electric field strength times the conductivity $j = \sigma E$ (Boerner and Holladay, 1990).

In Christensen (2002), the half-space sensitivity function was used as a weighting function in the mapping from a 1D conductivity structure to apparent conductivity based on an adaptive principle, i.e., to use a half-space conductivity for the weighting function equal to the apparent conductivity of the response. At any delay time, the step response of any layered structure is — per definition — the half-space response of the configuration used for the apparent conductivity at that delay time. The approximate forward mapping was then used in a standard inversion formulation to produce a fast inversion procedure which, despite being approximate, is surprisingly accurate, the deviation from full-accuracy modeling being only approximately 5% on average (Christensen et al., 2009).

DISCUSSION

The half-space sensitivity functions of this paper are strictly valid only for this model, but they may serve as reasonable guidelines for more complicated earth models, and with some care, the results can be generalized to other system configurations.

The 3D sensitivity distribution of a given configuration reveals its fundamental characteristics, i.e., the way changes in subsurface conductivity structure will be manifest in the measured data. However, as demonstrated by Gomez-Trevino (1987a, 1987b), the sensitivity functions also serve as weighting functions directly between the conductivity distribution itself and the measured data, most represented through the apparent conductivity. With this in mind, the sensitivity functions provide a rich and detailed qualitative insight into the fundamental assets and limitations of any TEM configuration, an understanding that is necessary for system design and a critical appreciation of modeling and inversion results.

CONCLUSIONS

The most important characteristics of the TEM sensitivity functions can be summarized as follows:

- Impulse response sensitivity functions have one more sign change than the step response functions, but otherwise they have approximately the same lateral and vertical extent.
- The sensitivity function for the x -component is in general considerably more complicated than that of the z -component, and the sensitivity function of the offset loop configuration is more complicated than of a more compact configuration such as the central loop configuration.
- The lateral extent of the sensitivity distribution increases with Tx height for a constant ratio between delay time and conductivity t/σ , and for a constant half-space conductivity and height, it increases with time, reflecting the diffusion of the EM fields.
- The lateral 1D sensitivity functions for x -component data essentially performs a lateral differentiation of the conductivity

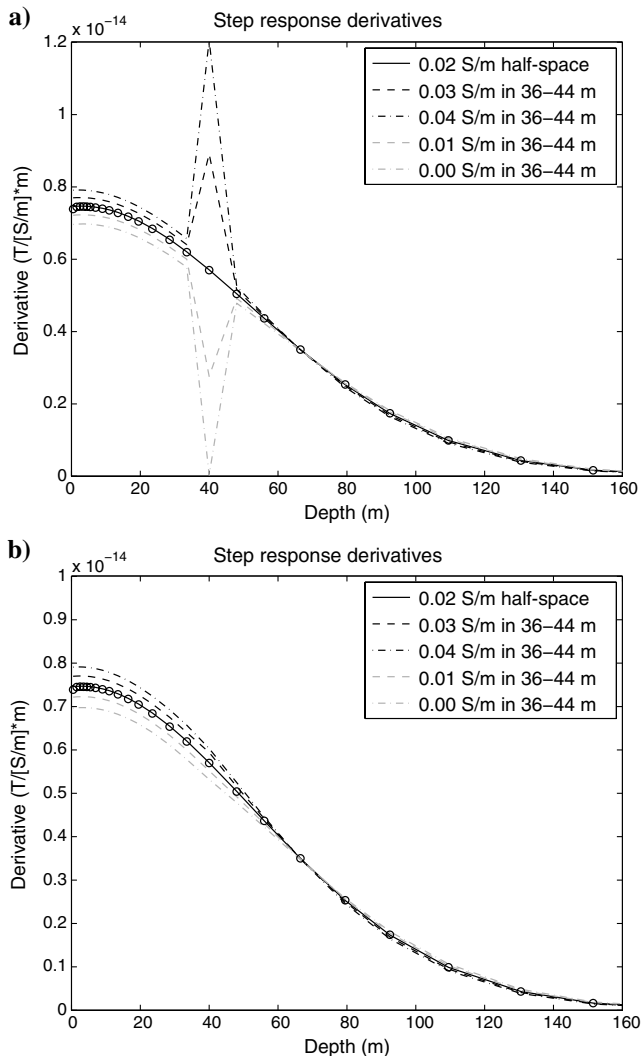


Figure 12. Step response derivatives for five 1D models: a homogeneous half-space with a conductivity of 0.02 S/m and four models with a perturbed conductivity of 0.03, 0.04, 0.01, and 0.0001 S/m in the depth range 36–44 m. (a) No scaling with perturbed conductivity. The configuration is an airborne central loop configuration at a height of 30 m with a Tx radius of 10 m and the delay time is 160 μs . (b) Scaled with perturbed conductivity together with the derivatives calculated using the 1D sensitivity function (open circles).

structure along the measured profile. For the detection of lateral conductivity changes, the x -component is, therefore, superior to the z -component, but for the same reason, one should only include x -component data in a 1D inversion if the geologic setting is quite close to a true 1D situation.

Surprisingly, considering the differences between the 3D sensitivity functions of different Tx-Rx configurations, the step response 1D vertical sensitivity functions are quite similar.

Simple footprint measures can be defined based on 3D, 2D, and 1D sensitivity functions by outlining the width of the part of the sensitivity function that exceeds a relative absolute value of, e.g., 10% (or another arbitrary value). A footprint measure was thus defined from the 3D sensitivity function of a central loop configuration as a function of height. However, for more complicated sensitivity distributions with positive and negative sensitivities of the same order of magnitude, such as for the x -component of the central loop system and z - and x -components of offset configurations, a simple footprint measure has little informative value.

The 1D, 2D, and 3D sensitivity functions for the homogeneous half-space can be calculated quite rapidly and lend themselves easily to numerical integration over the volumes of a discretized model to provide approximate derivatives to be used in inversion procedures with 2D or 3D models with limited conductivity contrasts.

APPENDIX A

THE ELECTRIC FIELD WITHIN A HOMOGENEOUS HALF-SPACE INDUCED BY A VERTICAL-MAGNETIC-DIPOLE SOURCE AND A CIRCULAR LOOP

In the quasistatic approximation, the electric field within a homogeneous and isotropic half-space due to a magnetic-dipole source can be calculated using standard methods (Ward and Hohmann, 1987). Presented below are equations for a dipole source of moment M located at a height h above the surface of a half-space of conductivity σ .

In the frequency domain, for a vertical-magnetic-dipole source oriented in the positive z -direction, the total-electric field within the half-space $E_\theta(r, z, \omega)$ has radial symmetry with respect to the z -axis. In cylindrical coordinates the azimuthal component of the electric field is given by

$$E_\theta(r, z, \omega) = -\frac{i\omega\mu M}{2\pi} \int_0^\infty \frac{\lambda^2}{\lambda + u} e^{-\lambda h} e^{-uz} J_1(\lambda r) d\lambda, \quad (\text{A-1})$$

where ω is the angular frequency, μ_0 is the free-space magnetic permeability, λ is the free-space wavenumber, $u = \sqrt{\lambda^2 + i\omega\mu_0\sigma}$ is the wavenumber in the half-space, and $J_1(\lambda r)$ is the first-order Bessel function.

In the case of a horizontal circular transmitter loop of radius a , the electric field is given by the dipole expression multiplied with the factor $J_1(\lambda a)/[(1/2)\lambda a]$:

$$E_\theta(r, z, \omega) = -\frac{i\omega\mu M}{2\pi} \int_0^\infty \frac{\lambda^2}{\lambda + u} e^{-\lambda h} e^{-uz} \frac{J_1(\lambda a)}{(1/2)\lambda a} J_1(\lambda r) d\lambda. \quad (\text{A-2})$$

Projection onto the x - and y -axes yields the Cartesian components:

$$\begin{aligned} E_x(r, z, \omega) &= -\frac{y}{r} E_\theta(r, z, \omega) \quad \text{and} \\ E_y(r, z, \omega) &= \frac{x}{r} E_\theta(r, z, \omega). \end{aligned} \quad (\text{A-3})$$

For $z = 0, h = 0$, an analytical solution exists for the integral in equation A-1 (Ward and Hohmann, 1987). However, in the general case, the Hankel transforms in equations A-1 and A-2 can only be evaluated numerically. The calculations are performed using the optimized fast Hankel transform filter coefficients of Christensen (1990).

The time-domain expression corresponding to equation A-1 is given by an inverse Fourier transform:

$$\begin{aligned} e_\theta(r, z, t) &= -\frac{\mu M}{2\pi} \frac{d}{dt} \int_0^\infty \left[\frac{1}{2\pi} \int_{-\infty}^\infty \frac{e^{-uz}}{\lambda + u} e^{i\omega t} d\omega \right] \\ &\quad \times \lambda^2 e^{-\lambda h} J_1(\lambda r) d\lambda. \end{aligned} \quad (\text{A-4})$$

Let us consider the Fourier integral in the brackets. By the substitution $i\omega \rightarrow s$, the Fourier transform is expressed as an inverse Laplace transform:

$$\begin{aligned} F &= \frac{1}{2\pi} \int_{-\infty}^\infty \frac{e^{-uz}}{\lambda + u} e^{i\omega t} d\omega \\ &= \frac{1}{2\pi i} \int_{-i\infty}^{i\infty} \frac{\exp(-z\sqrt{\lambda^2 + \mu\sigma s})}{\lambda + \sqrt{\lambda^2 + \mu\sigma s}} e^{st} ds. \end{aligned} \quad (\text{A-5})$$

With the change of variable

$$\lambda^2 + \mu\sigma s = \mu\sigma s', \quad ds = ds', \quad s = s' - \lambda^2/\mu\sigma, \quad (\text{A-6})$$

we have

$$\begin{aligned} F &= \frac{1}{2\pi i} \int_{\frac{i^2}{\mu\sigma} - i\infty}^{\frac{i^2}{\mu\sigma} + i\infty} \frac{\exp(-z\sqrt{\mu\sigma}\sqrt{s'})}{\lambda + \sqrt{\mu\sigma}\sqrt{s'}} e^{s't} e^{-\frac{i^2}{\mu\sigma}t} ds' \\ &= \frac{1}{\sqrt{\mu\sigma}} e^{-\frac{i^2}{\mu\sigma}t} \cdot \frac{1}{2\pi i} \int_{\frac{i^2}{\mu\sigma} - i\infty}^{\frac{i^2}{\mu\sigma} + i\infty} \frac{\exp(-z\sqrt{\mu\sigma}\sqrt{s'})}{\lambda/\sqrt{\mu\sigma} + \sqrt{s'}} e^{s't} ds'. \end{aligned} \quad (\text{A-7})$$

Abramovitz and Stegun (1972, formula 29.3.88) give the inverse Laplace transform:

$$\begin{aligned} \mathcal{L}^{-1} \left(\frac{e^{-k\sqrt{s}}}{a + \sqrt{s}} \right) &= \frac{1}{\sqrt{\pi t}} \exp \left(-\frac{k^2}{4t} \right) \\ &\quad - ae^{ak} e^{a^2 t} \operatorname{erfc} \left(a\sqrt{t} + \frac{k}{2\sqrt{t}} \right), \end{aligned} \quad (\text{A-8})$$

whereby

$$\begin{aligned}
F &= \frac{1}{\sqrt{\mu\sigma}} e^{\frac{z^2}{4t}} \left[\frac{1}{\sqrt{\pi t}} e^{-\frac{z^2}{4t}} \right. \\
&\quad \left. - \frac{\lambda}{\sqrt{\mu\sigma}} e^{\frac{\lambda}{\sqrt{\mu\sigma}} z \sqrt{\mu\sigma}} e^{\frac{z^2}{4t}} \operatorname{erfc} \left(\lambda \sqrt{t/\mu\sigma} + \frac{z}{2} \sqrt{\mu\sigma/t} \right) \right] \\
&= \frac{1}{\mu\sigma\tau\sqrt{\pi}} e^{-(\lambda\tau)^2} e^{-\left(\frac{z}{2\tau}\right)^2} \\
&\quad \times \left[1 - \lambda\tau\sqrt{\pi} e^{(\lambda\tau+z/2\tau)^2} \operatorname{erfc} \left(\lambda\tau + \frac{z}{2\tau} \right) \right], \quad (\text{A-9})
\end{aligned}$$

with $\tau = \sqrt{t/\mu\sigma}$. The function $\exp(x^2) \cdot \operatorname{erfc}(x)$ can be calculated in a numerically stable fashion, e.g., through the series expansion from Abramowitz and Stegun (1972, formula 7.1.26).

Neglecting the differentiation d/dt , the e -field from the step (step-on) response is given as

$$\begin{aligned}
e_{\theta}(r, z, t) &= -\frac{M}{2\pi} \frac{1}{\sigma\tau\sqrt{\pi}} \int_0^{\infty} e^{-(\lambda\tau)^2} e^{-\left(\frac{z}{2\tau}\right)^2} \\
&\quad \times \left[1 - \lambda\tau\sqrt{\pi} e^{(\lambda\tau+z/2\tau)^2} \operatorname{erfc} \left(\lambda\tau + \frac{z}{2\tau} \right) \right] \\
&\quad \cdot \lambda^2 e^{-\lambda h} J_1(\lambda r) d\lambda. \quad (\text{A-10})
\end{aligned}$$

The step response (step-off) is given by $e_{-}(t) = e(\infty) - e(t)$ and because $e(\infty) = 0$, we have

$$\begin{aligned}
e_{\theta}(r, z, t) &= \frac{M}{2\pi} \frac{1}{\sigma\tau\sqrt{\pi}} \int_0^{\infty} e^{-(\lambda\tau)^2} e^{-\left(\frac{z}{2\tau}\right)^2} \\
&\quad \times \left[1 - \lambda\tau\sqrt{\pi} e^{(\lambda\tau+z/2\tau)^2} \operatorname{erfc} \left(\lambda\tau + \frac{z}{2\tau} \right) \right] \\
&\quad \cdot \lambda^2 e^{-\lambda h} J_1(\lambda r) d\lambda. \quad (\text{A-11})
\end{aligned}$$

APPENDIX B

CONVOLUTION AS NUMERICAL INTEGRATION

Instead of calculating the convolution between the time-domain components of the electric field, equation 3, as a discrete convolution of equidistantly sampled values, the convolution can be calculated as a numerical integration of a function given by its discrete values:

$$h(t) = \int_0^t f(t')g(t'-t)dt'. \quad (\text{B-1})$$

In the initial calculations, the functions f and g are sampled logarithmically, but in the convolution integral B-1, the function g is inverted and the two functions are no longer sampled at the same points, so they have to be resampled. In the first half of the interval $[0; t]$, f is sampled densely, whereas g is sampled more sparsely, and vice versa in the second half of the interval. The f needs to be resampled at the sample points of g in the last half of the interval, and g needs to be resampled at the sample points of f in the first half of the interval. This is illustrated in Figure B-1.

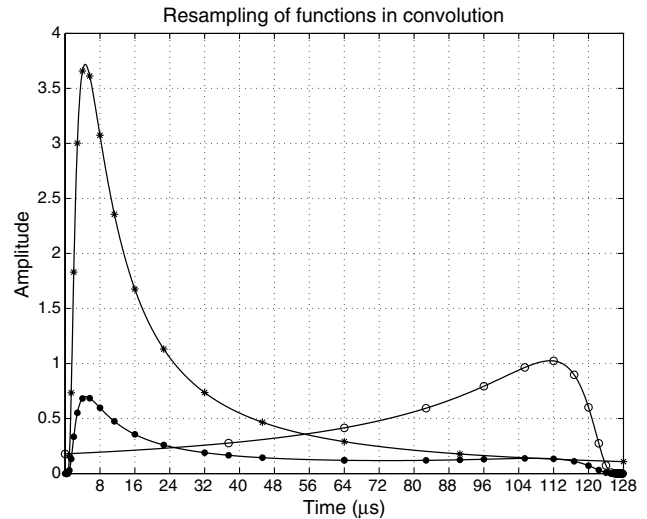


Figure B-1. The figure illustrates the sampling of the functions $f(t')$ (samples indicated by stars) and $g(t'-t)$ (samples indicated by open circles) and their product $f(t')g(t'-t)$ (samples indicated by filled circles) of equation B-1 for the delay time $t = 128 \mu\text{s}$. The amplitude is arbitrary.

In the practical implementation, it is advantageous to choose the sampling density as defined by a certain number of samples per octave (and not per decade) because that ensures that the midpoint of the time interval $[0; t]$ is a sampling point for f and g .

For each delay time t , the principle steps of the computations are as follows:

- 1) Choose the earliest time t_e to be sampled and the sampling density as several samples per octave N_{oct} .
- 2) With this choice of logarithmic sampling, compute the functions f and g using the fast Hankel transform filters of Christensen (1990) using equation A-11.
- 3) Compute the product $f(t')g(t'-t)$, resampling the functions as suggested above.
- 4) Assuming the product to be represented by third degree local splines between the sample points, perform an analytic integration of the splines; the total integral can then be expressed through the spline coefficients.

The calculation should not start with the very earliest time $t = t_e$ because the functions will be insufficiently sampled. Starting with the delay time t_i , $i = 2 \cdot N_{\text{oct}}$ will ensure that there are enough samples at the earliest delay time to give an acceptable accuracy.

In the calculations of this paper, the sampling density was chosen as 2/octave, corresponding to ~ 6.5 samples per decade in time, corresponding to ~ 13 samples per decade in space, and the earliest time was chosen as $t_e = 10 \text{ ns}$.

REFERENCES

- Abramowitz, M., and I. A. Stegun, 1972, Handbook of mathematical functions, 9th ed.: National Bureau of Standards.
- Auken, E., L. Pellerin, N. B. Christensen, and K. I. Sørensen, 2006, A survey of current trends in near-surface electrical and electromagnetic methods: Geophysics, 71, no. 5, G249–G260, doi: 10.1190/1.2335575.
- Auken, E., S. Violette, N. d'Ozouville, B. Deffontaines, K. I. Sørensen, A. Viezzoli, and G. de Marsily, 2009, An integrated study of the hydrogeology of volcanic islands using helicopter borne transient electromagnetic:

- Application in the Galápagos Archipelago: *Comptes Rendus Geosciences*, **341**, 899–907, doi: [10.1016/j.crte.2009.07.006](https://doi.org/10.1016/j.crte.2009.07.006).
- Beamish, D., 2003, Airborne EM footprints: *Geophysical Prospecting*, **51**, 49–60, doi: [10.1046/j.1365-2478.2003.00353.x](https://doi.org/10.1046/j.1365-2478.2003.00353.x).
- Beamish, D., and A. Mattsson, 2003, Time lapse airborne EM surveys across a municipal landfill: *Journal of Environmental and Engineering Geophysics*, **8**, 157–165, doi: [10.4133/JEEG8.3.157](https://doi.org/10.4133/JEEG8.3.157).
- Boerner, D. E., and J. S. Holladay, 1990, Approximate Fréchet derivatives in inductive electromagnetic soundings: *Geophysics*, **55**, 1589–1595, doi: [10.1190/1.1442810](https://doi.org/10.1190/1.1442810).
- Chave, A. D., 1984, The Fréchet derivatives of electromagnetic induction: *Journal of Geophysical Research*, **89**, 3373–3380, doi: [10.1029/JB089iB05p03373](https://doi.org/10.1029/JB089iB05p03373).
- Christensen, N. B., 1990, Optimized fast Hankel transform filters: *Geophysical Prospecting*, **38**, 545–568, doi: [10.1111/j.1365-2478.1990.tb01861.x](https://doi.org/10.1111/j.1365-2478.1990.tb01861.x).
- Christensen, N. B., 1995, Imaging of central loop transient electromagnetic soundings: *Journal of Environmental and Engineering Geophysics*, **1**, 53–66, doi: [10.4133/JEEG1.A.53](https://doi.org/10.4133/JEEG1.A.53).
- Christensen, N. B., 1997, Electromagnetic subsurface imaging — A case for an adaptive Born approximation: *Surveys in Geophysics*, **18**, 477–510, doi: [10.1023/A:1006593408478](https://doi.org/10.1023/A:1006593408478).
- Christensen, N. B., 2002, A generic 1-D imaging method for transient electromagnetic data: *Geophysics*, **67**, 438–447, doi: [10.1190/1.1468603](https://doi.org/10.1190/1.1468603).
- Christensen, N. B., and J. Reid, 2011, Defining formation boundaries in multi-layer models through statistical analysis: Presented at Near Surface 2011 — The 17th European Meeting of Environmental and Engineering Geophysics.
- Christensen, N. B., J. E. Reid, and M. Halkjær, 2009, Fast, laterally smooth inversion of airborne time-domain electromagnetic data: *Near Surface Geophysics*, **7**, 599–612, doi: [10.3997/1873-0604.2009047](https://doi.org/10.3997/1873-0604.2009047).
- Fitterman, D. V., and M. Deszcz-Pan, 1998, Helicopter EM mapping of salt-water intrusion in Everglades National Park, Florida: *Exploration Geophysics*, **29**, 240–243, doi: [10.1071/EG98240](https://doi.org/10.1071/EG98240).
- Gomez-Trevino, E., 1987a, Nonlinear integral equations for electromagnetic inverse problems: *Geophysics*, **52**, 1297–1302, doi: [10.1190/1.1442390](https://doi.org/10.1190/1.1442390).
- Gomez-Trevino, E., 1987b, A simple sensitivity analysis of time-domain and frequency-domain electromagnetic measurements: *Geophysics*, **52**, 1418–1423, doi: [10.1190/1.1442254](https://doi.org/10.1190/1.1442254).
- Gomez-Trevino, E., F. Esparza, and S. Méndez-Delgado, 2002, New theoretical and practical aspects of electromagnetic soundings at low induction numbers: *Geophysics*, **67**, 1441–1451, doi: [10.1190/1.1512744](https://doi.org/10.1190/1.1512744).
- Hammack, R. W., G. A. Veloski, J. I. Sams, and G. S. Mable, 2002, The use of airborne EM conductivity to locate contaminant flow paths at the Sulphur Bank Mercury mine superfund site: Presented at 15th EEGS Symposium on the Application of Geophysics to Engineering and Environmental Problems.
- Hördt, A., 1998, Calculation of electromagnetic sensitivities in the time domain: *Geophysical Journal International*, **133**, 713–720, doi: [10.1046/j.1365-246X.1998.00533.x](https://doi.org/10.1046/j.1365-246X.1998.00533.x).
- Jørgensen, F., W. Scheer, S. Thomson, T. O. Sonnenborg, K. Hinsby, H. Wiederhold, C. Schamper, T. Burschil, B. Roth, R. Kirsch, and E. Auken, 2012, Transboundary geophysical mapping of geological elements and salinity distribution critical for the assessment of future sea water intrusion in response to sea level rise: *Hydrology and Earth System Sciences*, **16**, 1845–1862, doi: [10.5194/hess-16-1845-2012](https://doi.org/10.5194/hess-16-1845-2012).
- Kirkegaard, C., N. Foged, E. Auken, A. V. Christiansen, and K. I. Sørensen, 2012, On the value of including x -component data in 1D modeling of electromagnetic data from helicopterborne time domain systems in horizontally layered environments: *Journal of Applied Geophysics*, **84**, 61–69, doi: [10.1016/j.jappgeo.2012.06.006](https://doi.org/10.1016/j.jappgeo.2012.06.006).
- Kovacs, A., J. S. Holladay, and C. J. J. Bergeron, 1995, The footprint/altitude ratio for helicopter electromagnetic sounding of sea-ice thickness: Comparison of theoretical and field estimates: *Geophysics*, **60**, 374–380, doi: [10.1190/1.1443773](https://doi.org/10.1190/1.1443773).
- Lane, R., A. Green, C. Golding, M. Owers, P. Pik, C. Plunkett, D. Sattel, and B. Thorn, 2000, An example of 3D conductivity mapping using the TEM-PEST airborne electromagnetic system: *Exploration Geophysics*, **31**, 162–172, doi: [10.1071/EG00162](https://doi.org/10.1071/EG00162).
- Liu, G., and A. Becker, 1990, Two-dimensional mapping of sea-ice keels with airborne electromagnetics: *Geophysics*, **55**, 239–248, doi: [10.1190/1.1442832](https://doi.org/10.1190/1.1442832).
- Macnae, J., 2007, Developments in broadband airborne electromagnetics in the past decade, in B. Milkereit, Proceedings of Exploration 07, Fifth Decennial International Conference on Mineral Exploration, 387–398.
- McCracken, K. G., M. L. Orstaglio, and G. W. Hohmann, 1986, Minimization of noise in electromagnetic exploration systems: *Geophysics*, **51**, 819–832, doi: [10.1190/1.1442134](https://doi.org/10.1190/1.1442134).
- McGillivray, P. R., and D. W. Oldenburg, 1990, Methods for calculating Fréchet derivatives and sensitivities for the non-linear inverse problem: A comparative study: *Geophysical Prospecting*, **38**, 499–524, doi: [10.1111/j.1365-2478.1990.tb01859.x](https://doi.org/10.1111/j.1365-2478.1990.tb01859.x).
- McGillivray, P. R., D. W. Oldenburg, R. G. Ellis, and T. M. Habashy, 1994, Calculation of sensitivities for the frequency-domain electromagnetic problem: *Geophysical Journal International*, **116**, 1–4, doi: [10.1111/j.1365-246X.1994.tb02121.x](https://doi.org/10.1111/j.1365-246X.1994.tb02121.x).
- Munday, T., G. Walker, and C. Liddicoa, 2004, Application of airborne geophysical techniques to salinity issues in the riverland, South Australia: SA SMMS site summary report.
- Nyboe, N. S., F. Jørgensen, and K. I. Sørensen, 2010, Integrated inversion of TEM and seismic data facilitated by high penetration depths of a segmented receiver setup: *Near Surface Geophysics*, **8**, 467–473, doi: [10.3997/1873-0604.2010026](https://doi.org/10.3997/1873-0604.2010026).
- Nyboe, N. S., and K. I. Sørensen, 2012, Noise reduction in TEM: Presenting a bandwidth- and sensitivity-optimized parallel recording setup and methods for adaptive synchronous detection: *Geophysics*, **77**, no. 3, E203–E212, doi: [10.1190/geo2011-0247.1](https://doi.org/10.1190/geo2011-0247.1).
- Paine, J. G., 2003, Determining salinization extent, identifying salinity sources, and estimating chloride mass: *Water Resources Research*, **39**, 1059, doi: [10.1029/2001WR000710](https://doi.org/10.1029/2001WR000710).
- Pedersen, R., and S. Thompson, 1991, GEOTEM case history: Time domain electromagnetic prospecting methods, in M. N. Nabighian, and J. C. Macnae, eds., *Electromagnetic methods in applied geophysics*: SEG, 509–513.
- Pérez-Flores, M. A., S. Méendez-Delgado, and E. Gómez-Treviño, 2001, Imaging low-frequency and DC electromagnetic fields using a simple linear approximation: *Geophysics*, **66**, 1067–1081, doi: [10.1190/1.1487054](https://doi.org/10.1190/1.1487054).
- Reid, J., N. B. Christensen, and K. Godber, 2012, SkyTEM helicopter transient electromagnetic surveys of tailings dams: ASEG Extended Abstracts, **1**, 1–4, doi: [10.1071/ASEG2012ab276](https://doi.org/10.1071/ASEG2012ab276).
- Reid, J. E., A. Pfaffling, and J. Vrbancich, 2006, Airborne electromagnetic footprints in 1D earths: *Geophysics*, **71**, no. 2, G63–G72, doi: [10.1190/1.2187756](https://doi.org/10.1190/1.2187756).
- Reid, J. E., and J. Vrbancich, 2004, A comparison of the inductive-limit footprint of airborne electromagnetic configurations: *Geophysics*, **69**, 1229–1239, doi: [10.1190/1.1801939](https://doi.org/10.1190/1.1801939).
- Smith, R. S., and P. B. Keating, 1996, The usefulness of multicomponent, time-domain airborne electromagnetic measurements: *Geophysics*, **61**, 74–81, doi: [10.1190/1.1443958](https://doi.org/10.1190/1.1443958).
- Sørensen, K. I., and E. Auken, 2004, SkyTEM — A new high-resolution helicopter transient electromagnetic system: *Exploration Geophysics*, **35**, 194–202, doi: [10.1071/EG04194](https://doi.org/10.1071/EG04194).
- Spies, B. R., 1988, Local noise prediction filtering for central induction transient electromagnetic sounding: *Geophysics*, **53**, 1068–1079, doi: [10.1190/1.1442543](https://doi.org/10.1190/1.1442543).
- Spies, B. R., 1989, Depth of investigation in electromagnetic sounding methods: *Geophysics*, **54**, 872–888, doi: [10.1190/1.1442716](https://doi.org/10.1190/1.1442716).
- Thomsen, R., V. H. Søndergaard, and K. I. Sørensen, 2004, Hydrogeological mapping as a basis for establishing site-specific groundwater protection zones in Denmark: *Hydrogeology*, **12**, 550–562, doi: [10.1007/s10040-004-0345-1](https://doi.org/10.1007/s10040-004-0345-1).
- Tølbøll, R. J., and N. B. Christensen, 2007, The sensitivity functions of frequency-domain magnetic dipole-dipole systems: *Geophysics*, **72**, no. 2, F45–F56, doi: [10.1190/1.2409623](https://doi.org/10.1190/1.2409623).
- Vrbancich, J., and P. K. Fullagar, 2007, Improved seawater depth determination using corrected helicopter time-domain electromagnetic data: *Geophysical Prospecting*, **55**, 407–420, doi: [10.1111/j.1365-2478.2007.00602.x](https://doi.org/10.1111/j.1365-2478.2007.00602.x).
- Wang, G. L., C. Torres-Verdín, J. M. Salazar, and B. Voss, 2009, Fast 2D inversion of large borehole EM induction data sets with an efficient Fréchet-derivative approximation: *Geophysics*, **74**, no. 1, E75–E91, doi: [10.1190/1.3033213](https://doi.org/10.1190/1.3033213).
- Ward, S. H., and G. W. Hohmann, 1987, Electromagnetic theory for geophysical applications, in M. N. Nabighian, ed., *Electromagnetic methods in applied geophysics*, vol. 1: SEG Investigations in Geophysics, vol. 3, 131–311.
- Wolfgram, P., D. Sattel, and N. B. Christensen, 2003, Approximate 2D inversion of AEM data: *Exploration Geophysics*, **34**, 29–33, doi: [10.1071/EG03029](https://doi.org/10.1071/EG03029).
- Yin, C., and G. Hodges, 2005, Four dimensional visualization of EM fields for a helicopter EM system: 75th Annual International Meeting, SEG, Expanded Abstracts, 595–599.